

Evidence for magma-carbonate interaction beneath Syrtis Major, Mars

Timothy D. Glotch¹ and A. Deanne Rogers¹

Received 4 August 2012; revised 6 October 2012; accepted 5 November 2012; published 31 January 2013.

[1] We used three methods—spectral index mapping, linear spectral mixture analysis, and factor analysis and target transformation—to determine if carbonate decomposition products, including lime (CaO), periclase (MgO), portlandite (Ca(OH)₂), and brucite (Mg(OH)₂), are present on the surface of Mars. Using an expanded spectral library that includes decomposition products of calcite and magnesite, we deconvolved a binned emissivity data set from the Mars Global Surveyor Thermal Emission Spectrometer (MGS-TES). The deconvolution model indicates that anhydrous carbonates are not present at kilometer scales above the TES detection limit; however, carbonate decomposition products may be present at or above the TES detection limit in northeast Syrtis Major and several other small regions on Mars. The model results are supported by spectral index mapping and factor analysis and target transformation of TES data in this region. The volcanic setting of the detections may indicate the interaction of Syrtis Major lavas with subsurface carbonates, or, alternatively, the eruption of carbonate-bearing lavas that were subsequently devolatilized by impacts or later lava flows.

Citation: Glotch, T. D., and A. D. Rogers (2013), Evidence for magma-carbonate interaction beneath Syrtis Major, Mars, *J. Geophys. Res. Planets*, 118, 126–137, doi:10.1029/2012JE004230.

1. Introduction

[2] The question of whether carbonates ever formed on Mars at large outcrop scales has motivated remote sensing and in situ analyses of the Martian surface. Most previous work has focused on determining if sedimentary carbonates exist on Mars, as the widespread presence of carbonate outcrops would strongly imply local aqueous conditions with a neutral to alkaline pH. Previous analyses of Mars Global Surveyor (MGS) Thermal Emission Spectrometer (TES) data indicated that carbonates are not present at large outcrop scales on Mars with abundances above the TES detection limit of 10–15% [Bandfield, 2002]. Further detailed analysis of the TES data suggested that magnesite (MgCO₃) is present at the 2–5% level in the Martian globally homogenous fines, which likely formed in recent times as a result of a surface/atmosphere interaction [Bandfield et al., 2003; Boynton et al., 2009]. Although carbonate minerals are not a major component of surface materials at global/regional scales, local scale carbonate-bearing exposures have been identified (Figure 1). The discovery of magnesite outcrops in the Nili Fossae region of Mars using data from the Mars Reconnaissance Orbiter (MRO) Compact Reconnaissance

Imaging Spectrometer for Mars (CRISM) instrument suggests that carbonates also formed as a result of aqueous alteration of basaltic rocks during the Noachian [Ehlmann et al., 2008]. Brown et al. [2010] further suggest that the interbedded clay and carbonate deposits in Nili Fossae resulted from hydrothermal conditions. Michalski and Niles [2010] identified Ca- and Fe-bearing carbonates in layered/foliated bedrock within the central peak of Leighton crater, ~1500 km southwest of Nili Fossae, and suggested either metamorphism of phyllosilicate and carbonate-bearing surface sediments or CO₂-metasomatism of typical basaltic rocks to explain their presence. Additional deposits of Fe and Ca-bearing carbonates have been found south/southwest of Syrtis Major [Wray et al., 2011a, 2011b]. Carbonates have also been found in Gusev crater using the Mars Exploration Rover Spirit's Mössbauer, Mini-TES and APXS spectrometers [Morris et al., 2010]. The Mg-rich carbonates in the Comanche outcrop in the Columbia Hills likely formed from near-neutral pH hydrothermal alteration of ultramafic rocks. Recent searches for more widespread outcrop-scale carbonates on Mars focusing on potential paleolake basins [Orofino et al., 2009] have found no evidence for their presence [Stockstill et al., 2005, 2007].

[3] While carbonates are ubiquitous components of the Martian globally homogenous fines at the 2–5% level [Bandfield et al., 2003], the lack of widespread carbonate outcrops at the surface of Mars has led to the suggestion that Noachian atmospheric conditions prevented the precipitation of carbonates on the surface [Bullock and Moore, 2007; Halevy et al., 2007]. Others have suggested that carbonates that once formed on the surface of Mars are photochemically unstable under Martian conditions and that only oxides of

¹Department of Geological Sciences, Stony Brook University, Stony Brook, New York, USA.

Corresponding author: T. D. Glotch, Department of Geosciences, Stony Brook University, Stony Brook, NY 11794-2100, USA. (tglotch@notes.cc.sunysb.edu)

©2012. American Geophysical Union. All Rights Reserved. 2169-9097/13/2012JE004230

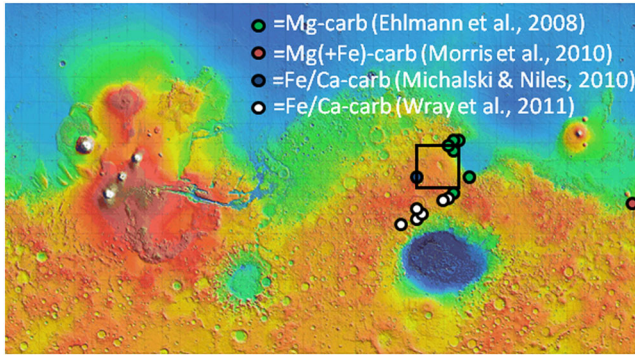


Figure 1. Map of reported carbonate detections on Mars. The black box outlines Syrtis Major. Adapted from Wray *et al.* [2011a].

the carbonate cations (e.g., CaO, MgO) would remain on the surface [Mukhin *et al.*, 1996]. Subsequent experiments, however, have generally shown carbonates to be stable under a variety of UV exposure conditions [Quinn *et al.*, 2006; Cloutis *et al.*, 2008; Stalport *et al.*, 2010].

[4] Pollack *et al.* [1987] suggested that a thick CO₂-rich atmosphere could have been maintained in the Noachian by abundant volcanic activity—either directly, through the injection of juvenile CO₂ into the atmosphere, or indirectly, through recycling of CO₂ into the atmosphere via the thermal decomposition of buried carbonates. It is also possible that carbonates could be decomposed by impact processes, although Carr [1989] suggests that this process is likely not as efficient as volcanism. Impact processes have been shown to have a strong effect on clay minerals in ancient Martian terrains [Che and Glotch, 2012; Sharp *et al.*, 2012; Friedlander *et al.*, 2012], and recent modeling has shown that ground temperatures surrounding a new impact crater can be as high as 1000 °C. These temperatures are more than high enough to decompose carbonates and can last for thousands of years [Abramov and Kring, 2005; Fairen *et al.*, 2010].

[5] A long-standing problem in the analysis of TES data at Mars is that satisfactory fits to the spectra from low-albedo surfaces are not possible without the inclusion of minor <10% abundances of carbonate minerals [e.g., Bandfield, 2002]. Use of carbonates in these models is problematic because carbonate mineral spectra have strong features between ~1400 and 1600 cm⁻¹, which are absent from low-albedo surfaces on Mars [Christensen *et al.*, 2001; Bandfield and Smith, 2003]. Because carbonate minerals cannot be used to satisfactorily explain previous modeled results, it is necessary to explore other possibilities. In this work, we added thermal emission spectra of carbonate decomposition products to a standard spectral library for spectral mixture analysis of TES data. These materials are spectrally similar to carbonates at long wavelengths (low wave numbers), but lack the short wavelength (~1400–1600 cm⁻¹) spectral features associated with the ν₃ carbonate asymmetric stretching mode [e.g., Lane and Christensen, 1997]. The analysis of our deconvolution models suggests the presence of carbonate decomposition products in the Syrtis Major region of Mars. We also employed additional spectral analysis techniques—spectral index mapping and factor analysis

and target transformation (FATT)—to examine Syrtis Major in more detail.

[6] All of the spectral analysis techniques that we employed indicate that the Syrtis Major shield volcano has an anomalous long wavelength spectral feature that is best explained by the presence of carbonate decomposition products. The geologic setting of the carbonate decomposition products suggests that they were formed when Hesperian lava flows from the Syrtis Major volcano assimilated and decomposed subsurface carbonates in the region.

[7] Syrtis Major is Early Hesperian in age and composed of lava flows that have been estimated to be ~0.5–1 km thick [Hiesinger and Head, 2004]. Crater counts indicate that the eastern Syrtis lava flows, which cover the rim of the Noachian Isidis impact basin, are slightly younger than those in western Syrtis. Wrinkle ridge patterns and topographic analysis of Syrtis Major suggest that portions of the summit collapsed and slid to the southeast, perhaps due to gravitational instabilities [Hiesinger and Head, 2004], or magma chamber inflation [Crumpler *et al.*, 1996]. Based on previous analyses using TES data, Syrtis Major is basaltic, with roughly equal proportions of plagioclase feldspar and clinopyroxene [Rogers and Christensen, 2007]. The high clinopyroxene concentration is also consistent with near-infrared spectroscopic analyses [Bibring *et al.*, 2005].

2. Data and Methods

[8] We first acquired laboratory thermal emission spectra of carbonate decomposition products. We then used three methods to investigate the possibility of decomposed carbonates on Mars: (1) spectral index mapping, (2) linear spectral mixture analysis of both a global binned TES emissivity map and individual TES orbits of interest, and (3) factor analysis and target transformation to isolate independently variable scene end-members within areas of interest identified by methods 1 and 2.

2.1. Acquisition of Emissivity Spectra

[9] The spectra of carbonates and carbonate decomposition products all have major spectral features at long wavelengths (~300–500 cm⁻¹; ~20–33 μm). Here we focus on calcite, magnesite, and their oxide and hydroxide

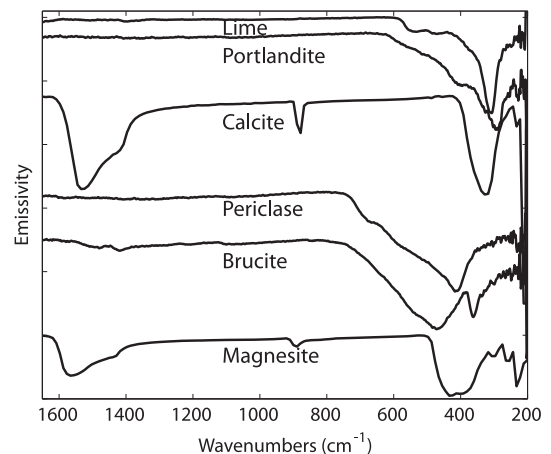


Figure 2. Emissivity spectra of calcium and magnesium carbonates, and their thermal decomposition products.

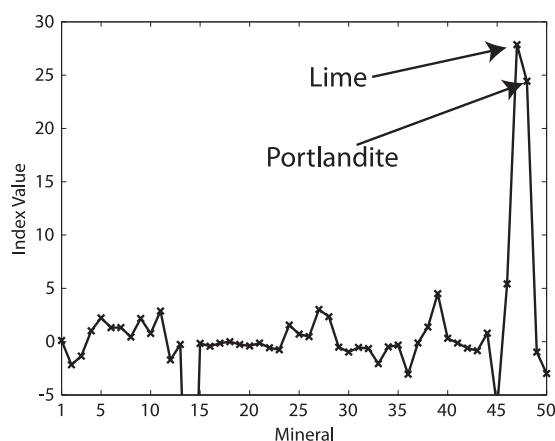


Figure 3. Comparison of index values for each mineral in our spectral library. Mineral index values are plotted in the order listed in Table 1.

decomposition products, lime, CaO , portlandite, Ca(OH)_2 , periclase, MgO , and brucite, Mg(OH)_2 (Figure 2). We acquired synthetic reagent-grade powders of periclase, brucite, and portlandite from Fisher Scientific. We prepared a sample of lime by heating reagent grade CaCO_3 powder to 850°C overnight. All powder samples were pressed into compact pellets at 12,000 psi in a Carver hydraulic press using a Pike Technologies 13 mm die and anvil set. Spectra were acquired in an atmosphere purged of CO_2 and H_2O on the Stony Brook University Vibrational Spectroscopy Laboratory's Nicolet 6700 Fourier transform infrared (FTIR) spectrometer modified to collect emissivity spectra similar to the methods described by *Ruff et al.* [1997]. All spectra are available in the Supporting Information and are also available on the Vibrational Spectroscopy Laboratory website at <http://aram.ess.sunysb.edu/tglotch/spectra.html>.

2.2. Spectral Index Mapping

[10] We produced a TES spectral index map that could indicate the presence of a long-wavelength spectral feature diagnostic of carbonate decomposition products. Spectral index maps have previously been generated from TES data to map the presence of hematite, dust, clays, and olivine [Christensen et al., 2000a; Ruff and Christensen, 2007; Koeppen and Hamilton, 2008; Michalski et al., 2010; Rogers and Ferguson, 2011]. We first prepared a global TES apparent emissivity map spanning all longitudes and -60° to 60°N latitude. High-quality, warm TES emissivity spectra with low water ice and dust signals covering Science Mapping Phase orbits 1–5317 were binned at a spatial resolution of 4 pixels per degree. The data cube was created using the methods described by Bandfield [2002], although ours differs slightly because we used the latest version of the TES calibration (version 002E). Of the 143 channels in a TES spectrum, only channels 9–35 and 65–110 (~ 233 – 508 and 825 – 1301 cm^{-1}) are commonly used for mineralogical analysis due to the presence of the fundamental atmospheric CO_2 feature centered at 667 cm^{-1} and minor atmospheric gas features and the low signal-to-noise ratio typically present in the TES spectra at shorter wavelengths. Using this standard 73-channel data cube, we then produced a spectral index

map indicative of lime or portlandite using the following equation:

$$I = (\epsilon_{265} + \epsilon_{497}) / (2 * \epsilon_{317}) - [(\epsilon_{381} + \epsilon_{497}) / (2 * \epsilon_{444})], \quad (1)$$

where ϵ_x denotes the emissivity at a particular TES wavelength. The first term in the formula indicates the presence or absence of an emissivity minimum associated with lime or portlandite. The second term is used to correct for misidentifications associated with hematite, which has a long-wavelength spectral feature close to those of lime and portlandite.

[11] The index was created from non-atmospherically corrected TES data, but makes use only of long-wavelength spectral features. At long wavelengths, the Martian atmosphere has a relatively low dust opacity, and atmospheric dust has a low spectral variability that will not substantially interfere with surface spectral features. While both water ice clouds and atmospheric water vapor have spectral features at long wavelengths, they result in index values that are negative or close to zero according to equation (1). Therefore, in this case, it is valid to create an index based on surface features in non-atmospherically corrected spectra. Anomalous high index values may still arise from spectra that have high atmospheric dust components, although we have guarded against this by carefully selecting the TES data that were used to create the binned emissivity cube.

[12] In general, spectral indices should be thought of as useful guides rather than exact maps. In some cases, multiple minerals can have high values for the same index. Figure 3 shows the index values of all 50 mineral spectra (normalized to have the same spectral contrast) in our spectral library. Lime has the highest index value, followed by portlandite. Other minerals with relatively high index values include siderite and hematite.

2.3. Factor Analysis and Target Transformation

[13] We used R-mode factor analysis and target transformation (FATT) techniques [Malinowski, 1991] to isolate any independently variable spectral shape that may be the cause of the spectral anomaly displayed in the index maps in Figure 3. The FATT technique can be used on any data set in which the components (1) vary independently of each other and (2) add linearly. Because the thermal infrared spectra of minerals have been shown to combine linearly for coarsely particulate surfaces [Gillespie, 1992; Thomson and Salisbury, 1993; Ramsey and Christensen, 1998], the TES and Mars Exploration Rover Mini-TES data sets are ideal for this type of analysis [e.g., Bandfield et al., 2000a; Glotch and Bandfield, 2006]. Syrtis Major is one of the darkest regions of Mars, with TES albedo values ranging from ~ 0.088 to ~ 0.150 . The low albedo suggests that the surface of Syrtis Major is composed of coarse rather than fine particulates. This interpretation is reinforced by the TES-derived thermal inertia [Mellon et al., 2000] for the region, which varies between ~ 175 and $275\text{ J m}^{-2}\text{ K}^{-1}\text{ s}^{-1/2}$. This correlates to an effective particle size of fine to medium sand [Presley and Christensen, 1997], which is well within the range of particle sizes for which mid-IR spectra have been shown to add linearly. One caveat is that we performed this analysis on TES data that were not atmospherically corrected; however, it has been shown that the combination of

Table 1. Library Mineral End-Members for Linear Spectral Mixture Analysis of TES Data^a

Mineral	Group	Mineral	Group
Quartz BUR-4120	Quartz	Olivine Fo68 KI3115 ^d	Olivine
Microcline BUR-3460	Feldspar	Olivine Fo35 KI3373 ^d	Olivine
Albite WAR-0235	Feldspar	Olivine Fo10 KI3008 ^d	Olivine
Oligoclase BUR-060D	Feldspar	Illite IMt-1	High-Si Phase
Andesine WAR-0024	Feldspar	Montmorillonite STx-1	High-Si Phase
Labradorite BUR-3080A	Feldspar	Saponite SpNv-1	High-Si Phase
Bytownite WAR-1384	Feldspar	Montmorillonite SWy-1	High-Si Phase
Anorthite BUR-340	Feldspar	K-rich glass ^e	High-Si Phase
Shocked An 17 GPa ^b	Feldspar	SiO ₂ glass ^e	High-Si Phase
Shocked An 21 GPa ^b	Feldspar	Opal-A 02-011 ^f	High-Si Phase
Shocked An 25.5 GPa ^b	Feldspar	Aluminous opal ^g	High-Si Phase
Shocked An 27 GPa ^b	Feldspar	Heulandite ^h	High-Si Phase
Shocked An 38.2 GPa ^b	Feldspar	Stilbite ^h	High-Si Phase
Shocked An 56.3 GPa ^b	Feldspar	Avg. Martian hematite ⁱ	Hematite
Bronzite NMNH-93527	Pyroxene	Anhydrite S9	Sulfate
Enstatite HS-9.4B	Pyroxene	Gypsum S6	Sulfate
Hypersthene NMNH-B18247	Pyroxene	Kieserite	Sulfate
Pigeonite ^c	Pyroxene	Calcite C40	Carbonate
Diopside	Pyroxene	Dolomite C20	Carbonate
Augite NMNH-9780 ^c	Pyroxene	Magnesite MAGBB-1 ^j	Carbonate
Augite NMNH-122302 ^c	Pyroxene	Siderite SIDIG-1 ^j	Carbonate
Hedenbergite DSM-HED01	Pyroxene	Lime ^j	Carb. Decomp.
Forsterite BUR-3720A	Olivine	Portlandite ^j	Carb. Decomp.
Fayalite WAR-RGFAY01	Olivine	Periclase ^j	Carb. Decomp.
Olivine Fo60 KI3362 ^d	Olivine	Brucite ^j	Carb. Decomp.

^aAll samples from the ASU spectral library available online at <http://tes.asu.edu> [Christensen et al., 2000b] unless otherwise noted.

^bJohnson et al. [2002].

^cProvided by V. E. Hamilton, described by Hamilton [2000].

^dDescribed by Morse [1996].

^eDescribed by Wyatt et al. [2001].

^fDescribed by Michalski et al. [2003].

^gProvided by M. D. Kraft.

^hDescribed by Ruff [2004].

ⁱDerived from TES data, described by Glotch et al. [2004].

^jThis study.

atmospheric and surface components behaves as an approximately linear system [Bandfield et al., 2000a], so use of this technique is justified.

[14] We began our analysis by gathering 10,000 high-quality, warm individual TES spectra acquired over orbits 1–5317 over the northern Syrtis Major region (65°–75°E, 6.5°–18.5°N). When using more than ~10,000 spectra, R-mode factor analysis becomes computationally prohibitive. However, it is desirable to use a large number of spectra, which improves the quality of the analysis by (1) reducing noise in the first several eigenvectors and (2) ensuring that the full variability present in the data set is captured. For both this analysis and spectral mixture analysis (section 2.4), we used the standard 73-channel TES data set described in section 2.2.

[15] Using this data set, we applied the R-mode factor analysis algorithm [Malinowski, 1991] to transform the spectra into a set of orthogonal, abstract eigenvectors with associated eigenvalues. The eigenvalues associated with each eigenvector represent the relative importance of each eigenvector to the total variability in the data set. The number of eigenvectors produced by the factor analysis process is equal to the number of spectral samples in the data set (73 for this work). However, the eigenvalues associated with the eigenvectors can be used to constrain which eigenvectors represent real variability in the data set and which simply represent noise. This has the beneficial effect of reducing the dimensionality and therefore complexity of large data sets.

[16] The eigenvectors that represent variability of non-noise components in the data set must be transformed back into physically meaningful components. To do this, we employ target transformation, which rotates the coordinate axes of the eigenvectors and aligns them to yield a physically meaningful result [Malinowski, 1991]. The eigenvectors are used to fit “target” spectra using a linear least squares routine, with a set of mineral and rock spectra as targets. If a mineral or rock spectrum is modeled well using the eigenvectors, then it is likely a component of the data set. Additional details on the FATT techniques can be found in Malinowski [1991], Bandfield et al. [2000a] and Glotch and Bandfield [2006].

2.4. Linear Least Squares Modeling of TES Data

[17] In addition to creating spectral index maps and FATT analysis, we performed linear deconvolution analyses on (1) the global TES emissivity data cube, (2) data from individual TES orbits over Syrtis Major, and (3) the FATT-derived spectra described in section 3.2. We used a spectral library consisting of the minerals shown in Table 1. The spectral library, in addition to the carbonate decomposition products, also includes a range of silicates, sulfates, and carbonates. All spectra are from the Arizona State University TES Spectral Library (<http://speclib.asu.edu>) unless otherwise noted. The library, which consists of mineral and atmospheric components [e.g., Bandfield, 2002; Bandfield et al., 2000a, 2000b; Rogers, 2011], was used to generate a linear least squares fit to the TES spectra. The atmospheric

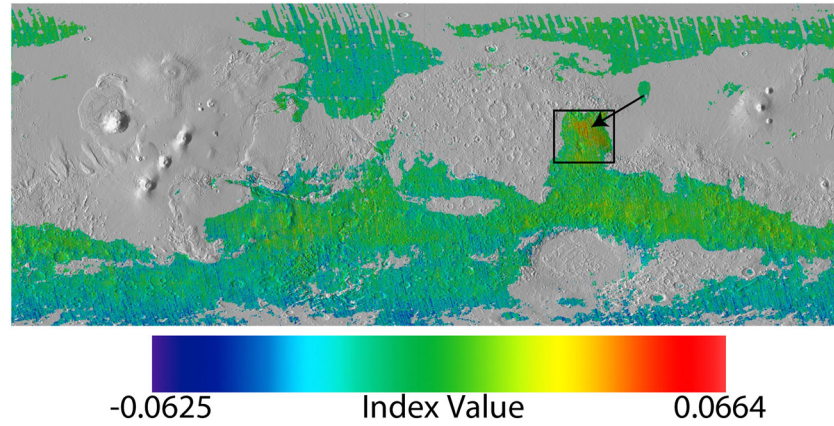


Figure 4. Global (-180° : 180° longitude; -60° : 60° latitude) TES lime/portlandite index map overlaid on a 4 pixels per degree Mars Orbiter Laser Altimeter (MOLA) shaded relief map. Pixels with TES albedo values >0.17 are masked out. Moderate index values are present throughout the southern highlands, but high values occur only in the vicinity of northeastern Syrtis Major (black arrow). The black box indicates the position of Figure 10a.

components were then scaled according to their modeled abundances and removed from the TES spectra to provide a surface emissivity spectrum. For the global emissivity cube analysis, we used the iterative deconvolution algorithm of *Ramsey and Christensen* [1998]. To deconvolve the individual Syrtis Major orbit and FATT spectra, we used the non-negative least squares algorithm of *Rogers and Aharonson* [2008]. This method has the advantage of always finding the global minimum error solution, and it is appropriate to deconvolve small numbers of spectra. However, this method is too computationally intensive for analysis of the many thousands of spectra in the global data set. In most cases, the iterative and non-negative least squares methods yield identical results [*Rogers and Aharonson*, 2008].

3. Results

3.1. Index Mapping

[18] A global TES lime/portlandite index map is shown in Figure 4. The map (Figure 4) has index values that range from -0.0625 to 0.0664 . Syrtis Major is the only large region on Mars with elevated index values. This region (65° – 75° E, 6.5° – 18.5° N) has an average index value of 0.0206 compared to a global average of -0.00004 . The standard deviation of the global index map is 0.0066 . Regions of slightly elevated index values also occur in Tyrrenna Terra, Terra Cimmeria, and Thaumasia Planum.

[19] This map suggests that there is a long-wavelength spectral feature in the TES data set that is geographically correlated with Syrtis Major. The average value for Syrtis Major is larger than the global average by >3 standard deviations.

3.2. Derivation of Scene-Derived Spectral End-Members

[20] We used the FATT algorithm on the standard 73-point TES data set covering Syrtis Major. The mean spectrum, first 10 eigenvectors, and associated eigenvalues are shown in Figure 5. The higher-order eigenvectors are dominated by noise rather than mineral or atmospheric spectral signatures, suggesting that the variability in the TES data set in this

region can be mostly accounted for by five to six independently variable spectral components. In some cases, minor components can be associated with higher order eigenvectors, making them difficult to completely separate from the noise [e.g., *Bandfield et al.*, 2002].

[21] Using this technique, we were able to recover five spectral end-members from the Syrtis Major region (Figure 6). These five spectral end-members compose the mean spectrum shown in Figure 5. The set of target vectors consisted of the Ca/Mg oxide and hydroxide spectra acquired

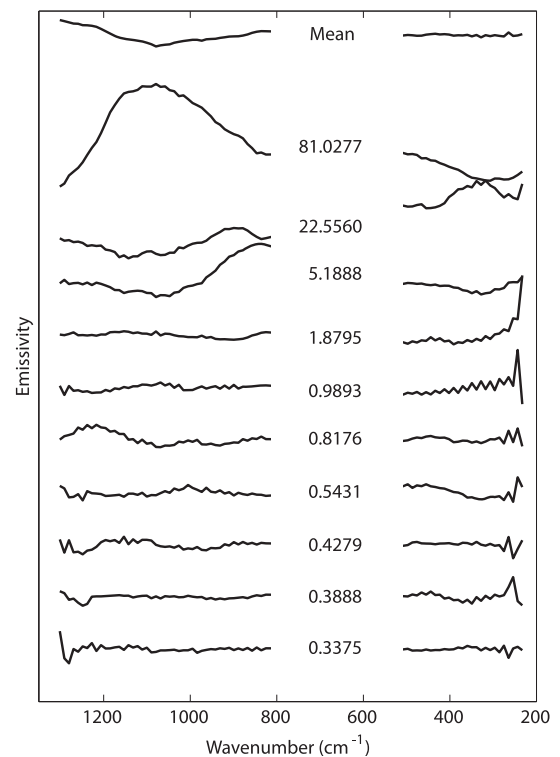


Figure 5. The mean and first 10 eigenvectors, and associated eigenvalues determined from the TES data set covering Syrtis Major. Eigenvector spectra are offset for clarity.

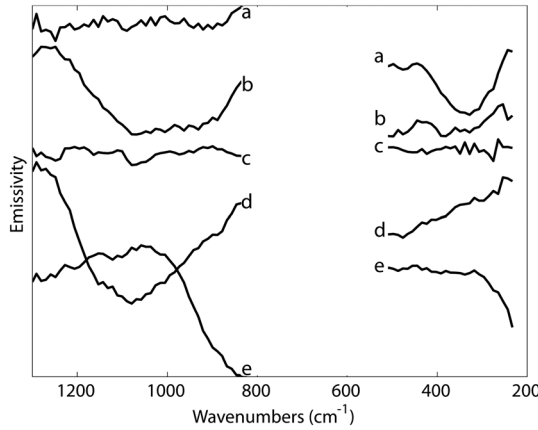


Figure 6. Recovered independently variable spectral components from Syrtis Major. Long-wavelength spectral feature consistent with (a) carbonate decomposition products, (b) basalt, (c) atmospheric CO₂, (d) atmospheric dust, and (e) atmospheric water vapor.

as part of this study, synthetic and derived atmospheric components from *Bandfield et al.* [2000a], ~100 mineral spectra from the Arizona State University TES Spectral Library (<http://speclib.asu.edu>), and an additional 100 spectra of rocks from the Wards Natural Science catalog. Mineral target spectra were from major mineral groups including silicates, oxides and hydroxides, carbonates, sulfates, and phosphates. Rock spectra included extrusive and intrusive igneous compositions with felsic to ultramafic compositions in addition to a variety of sedimentary and metamorphic rocks. Even though this large and diverse set of target vectors is not necessarily representative of the actual components in the TES data from this region, using a large library of target spectra allowed us to determine the independently variable spectral components and produce refined scene spectral end-members from a set of target vectors [e.g., *Bandfield et al.*, 2000a]. Using this large set of target vectors, we found a regional spectral shape (spectrum “a”) characterized by a deep long wavelength spectral feature and a relatively featureless spectrum between 800 and 1300 cm⁻¹ where, instead, silicates typically have strong features. We also recovered a regional basaltic spectral shape (spectrum “b”) similar to TES Type 1 [*Bandfield et al.*, 2000a, 2000b] or Group 2 [*Rogers et al.*, 2007], and three atmospheric spectral shapes representing atmospheric dust, atmospheric CO₂, and water ice clouds [*Bandfield and Smith*, 2003].

3.3. Spectral Mixture Analysis of TES Data

3.3.1. Spectral Mixture Analysis of the FATT-Derived Spectra

[22] The average FATT-derived spectrum with the anomalous long-wavelength spectral feature (Figure 6) is not a perfect match to a single mineral phase. We used the mineral end-members in our spectral library (Table 1) to deconvolve the FATT-derived spectrum to determine the most important mineral contributions to this spectrum. The FATT-derived and modeled spectra are shown in Figure 7, and the modeled mineralogy is shown in Table 2. The primary components of this spectral shape are carbonate decomposition products

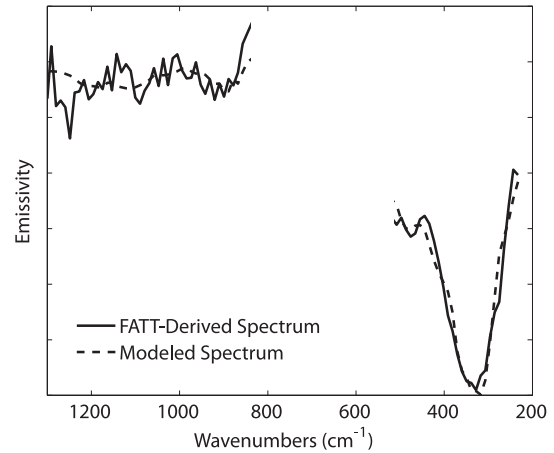


Figure 7. The FATT-derived spectrum showing the anomalous long-wavelength band (spectrum a from Figure 6) and the modeled spectrum determined by linear spectral mixture analysis. Results of the spectral mixture analysis are given in Table 2.

(~71%), carbonate (15%), and olivine (~11%), with negligible amounts of quartz and high-silica phases (Table 2). The major carbonate decomposition product used by the model is portlandite (~59%) followed by brucite (~12%).

[23] The FATT algorithm also recovered a spectral shape similar to the TES Group 2 spectral shape defined by *Rogers et al.* [2007]. The main difference is the overall higher emissivity of our FATT-derived spectral shape in the ~200–500 cm⁻¹ region as compared to the ST1 and Group 2 shapes (Figure 8a), although the long wavelength nature of this spectral shape is somewhat ambiguous. Because the FATT algorithm recovered an independent long-wavelength spectral shape, a basaltic shape could also be recovered with an arbitrary amount of the long-wavelength component added to or subtracted from it. With that caveat in place, spectral mixture analysis of the FATT-derived basaltic shape (Figure 8b and Table 3) shows that the primary constituents are feldspar (~38%), pyroxene (~31%), olivine (~11%), and high-silica phases (~10%), with negligible amounts of all other phases. *Rogers and Christensen* [2007] reported that the Group 2 spectral shape, which they found was prevalent mostly in Syrtis Major, is composed of pyroxene (33%), plagioclase (31%), high-silica phases (12%), olivine (7%), and 17% all other phases.

3.3.2. Spectral Mixture Analysis of the Global Data Set

[24] We performed a linear spectral mixture analysis of the binned TES emissivity data cube and summed the modeled abundances of (1) carbonates and (2) carbonate decomposition

Table 2. Results of the Spectral Mixture Analysis Model of the FATT-Derived Long-Wavelength Feature Spectrum From Syrtis Major

Mineral Group	Abundance (%)
Carbonate decomposition	70.8 ± 7.3
Carbonate	15.0 ± 4.3
Olivine	10.7 ± 4.2
Quartz	2.7 ± 2.3
High-silica phases	0.9 ± 5.1

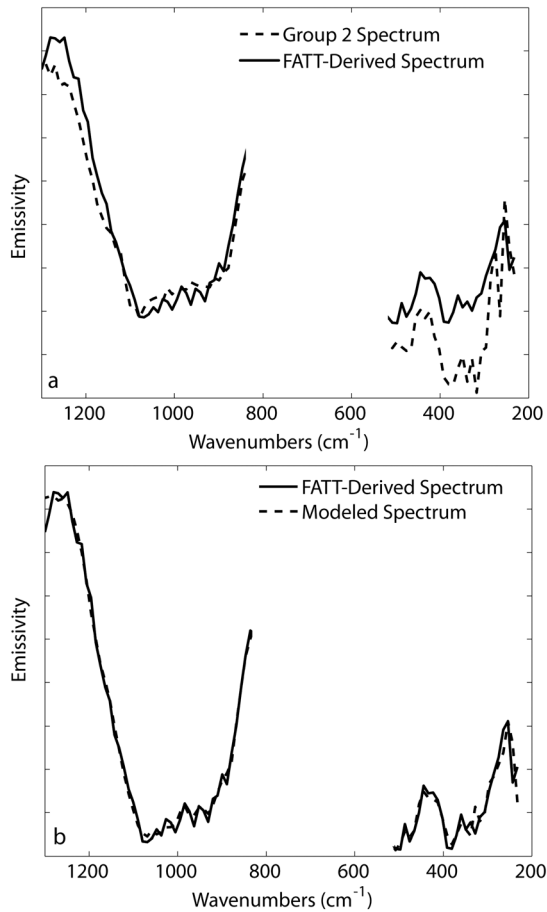


Figure 8. (a) Comparison of the Syrtis FATT-derived basalt shape with the Group 2 shape from *Rogers et al.* [2007]. The main difference occurs between 200 and 500 cm⁻¹. (b) Modeled Syrtis spectral shape. Derived mineral abundances are listed in Table 3.

products. The resulting abundance maps of each of these mineral groups determined by linear spectral mixture analysis are shown in Figure 9. The carbonate abundance map includes the summed abundances of calcite, dolomite, magnesite, and siderite. This map (Figure 9a) indicates that carbonates are not present over scales of tens of kilometers at abundances $\geq 5\%$. This result compares well with that of *Bandfield* [2002] as well as *Stockstill et al.* [2005, 2007] who also searched for their presence in TES data.

[25] The carbonate decomposition product abundance map is shown in Figure 9b. This map includes the summed abundances of lime, pericalse, portlandite, and brucite. Low concentrations are apparent over most of the planet, with the exception of Syrtis Major, and, perhaps, Terra Cimmeria, Tyrrhena Terra, and Thaumasia Planum. The average abundance of carbonate decomposition products over the entire surface of Mars is 3.2%, with a standard deviation of 2.2%. In Syrtis Major, between 67°–71°E and 10°–16°N, the average abundance is 7.2%, with several pixels in this region having abundances $>20\%$.

3.3.3. Spectral Mixture Analysis of Individual TES Orbits

[26] Our global deconvolution results, spectral index maps, and FATT analysis all suggest Syrtis Major has

unique spectral properties that may indicate the presence of carbonate decomposition products. As an additional test, we gathered data from four individual TES orbits from parts of Syrtis Major that showed variable index values in Figure 4. Figure 10a shows the positions of orbits 1902, 2015, 2191, and 2279 on the lime/portlandite index map. Figure 10b shows the average atmospherically corrected surface spectra and the model fits for each orbit using the mineral spectral library shown in Table 1. For these analyses, 230 individual TES spectra were averaged from orbit 1902, 105 spectra were averaged from orbit 2015, 172 spectra were averaged from orbit 2191, and 147 spectra were averaged from orbit 2279. Three of these orbits occur in an area with relatively high index values, while one (orbit 1902) occurs in a region that has lower average index value. Results of the analyses are given in Table 4. Carbonate decomposition product abundances range from $\sim 10\%$ to $\sim 16\%$ and are inversely correlated with modeled high-calcium pyroxene abundances, which range from $\sim 15\%$ to $\sim 28\%$, and modeled sulfate abundances, which range from 1.6% to 9.5%. In each case, the only modeled carbonate decomposition product is portlandite. Abundances of feldspar, olivine, and high-silica phases are consistent with the generally basaltic character of the region and are comparable to previous estimates [e.g., *Rogers and Christensen*, 2007].

5. Discussion

[27] Each of the three methods we employ—spectral index mapping, factor analysis and target transformation, and spectral mixture analysis—indicates the presence of a long wavelength spectral feature in the TES data covering Syrtis Major. This long-wavelength feature is consistent with the presence of carbonates or the products of their decomposition, and no other mineral or mineral class has been identified that can account for this spectral feature.

[28] *Mustard et al.* [1993] suggested, based on ISM data, that the mafic composition of Syrtis Major is relatively homogenous and that the observed spectral variability from west to east is due to the addition of a ferric dust coating or duricrust in eastern Syrtis. *Rogers et al.* [2007] noted that Syrtis Major is spectrally distinct from other low-albedo surfaces in TES data, and *Rogers and Christensen* [2007] found that, based on TES data, the characteristic Syrtis spectral shape is dominated by plagioclase feldspar (31%) and high-Ca clinopyroxene (29%), with smaller amounts of high-silica phases and other minerals. This result is broadly consistent with VNIR studies, which also found that the composition of Syrtis Major is dominated by high-Ca

Table 3. Results of the Spectral Mixture Analysis Model of the FATT-Derived Basaltic Spectrum From Syrtis Major

Mineral Group	Abundance
Feldspar	37.8 ± 3.3
Pyroxene	30.7 ± 3.1
Olivine	11.0 ± 1.8
High-silica phases	10.4 ± 2.6
Sulfate	4.1 ± 1.1
Carbonate decomposition products	3.0 ± 1.4
Quartz	2.2 ± 0.4
Carbonate	0.8 ± 0.4

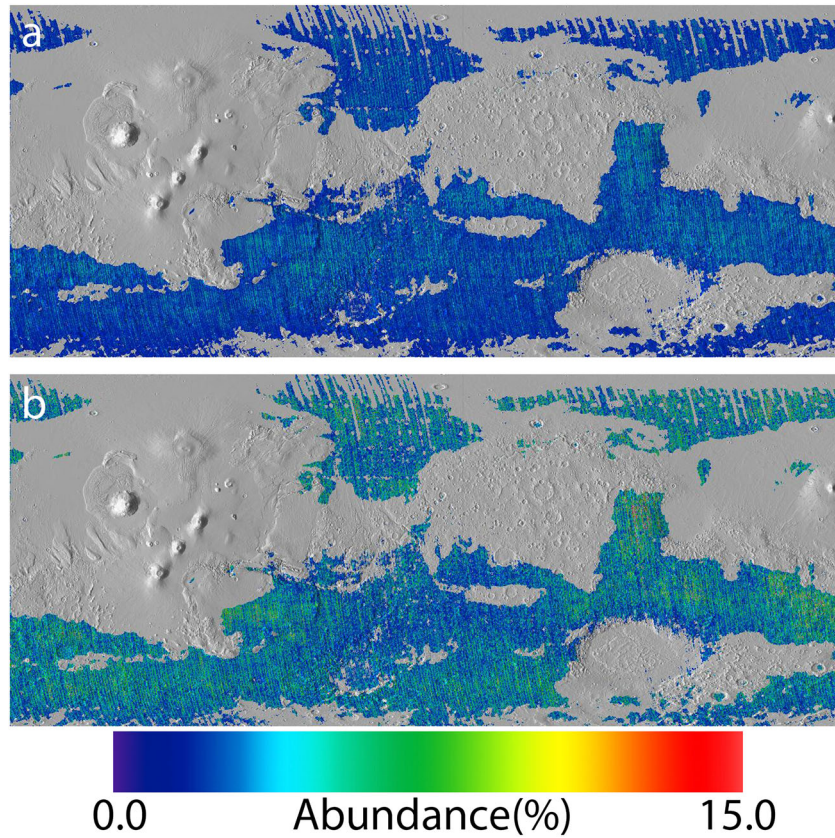


Figure 9. Global abundance maps of (a) carbonates and (b) carbonate decomposition products determined using linear spectral mixture analysis.

clinopyroxene [Bibring *et al.*, 2005]. Our results are also broadly consistent with those of Rogers and Christensen [2007]. Overall, plagioclase and clinopyroxene values are slightly lower, and carbonate decomposition product abundances are $\sim 15\%$ (Table 4) in the high index value region shown in Figures 4 and 10 (note that the carbonate decomposition product abundances are derived from deconvolution of both binned and individual TES orbit data, rather than deconvolution of the FATT-derived spectral shape shown in Figure 7).

[29] The source of the original carbonates that were decomposed to produce the unique spectral feature we see in Syrtis Major (Figures 6 and 7) is ambiguous, but we hypothesize that deeply buried sedimentary or hydrothermal carbonates interacted with Syrtis Major magmas during their ascent to the surface. These carbonates were devolatilized and/or assimilated into the Syrtis magmas, and the resulting products were eventually exposed on the surface.

[30] Recent work has shown that deeply buried carbonates have been exposed by erosion and impact processes in circum-Nili/Isidis region and south and west of Syrtis Major (Figure 1) [Ehlmann *et al.*, 2008; Michalski and Niles, 2010; Wray *et al.*, 2011a; Ehlmann and Mustard, 2012]. These are primarily Mg- and Ca/Fe-bearing carbonates, while this study indicates that decomposition products found at Syrtis Major are primarily derived from Ca-bearing carbonates. Michalski and Niles [2010] and Wray *et al.* [2011a] proposed that there may be a regional buried carbonate layer, and J. R. Michalski *et al.* (manuscript in

review, 2013) have proposed that these deeply buried carbonates were formed by brine metasomatism, perhaps as a result of ancient surface waters percolating through the regolith and altering rocks at depth [e.g., Niles *et al.*, 2005]. Alternatively, Viviano *et al.* [2012] suggest carbonation of serpentine as a method for forming carbonate. Regardless of the formation pathway of the carbonates exposed in this area, the fact that a number of carbonate exposures have been identified in both impact craters and tectonic/erosional troughs in the region points to a widespread regional deposit. The Syrtis Major volcanic complex covers an area $> 1.2 \times 10^6 \text{ km}^2$ and is composed of lavas with a volume of $\sim 1.6\text{--}3.2 \times 10^5 \text{ km}^3$ [Hiesinger and Head, 2004]. These lavas alone would be enough to bury a regional surficial carbonate deposit, but because they are Hesperian in age, it is likely that older Noachian lavas first covered the carbonates, if, in fact, they formed on the surface.

[31] It is highly likely that these carbonates formed in the early-to-mid Noachian. Ehlmann *et al.* [2008] found that the Mg-bearing carbonates exposed in Nili Fossae, just northeast of Syrtis Major, are restricted to Noachian terrain, lying stratigraphically above a clay-bearing layer and below a sulfate-bearing layer [Ehlmann and Mustard, 2012]. Niles *et al.* [2005] proposed a brine metasomatism model of carbonate formation requiring the percolation of CO_2 -rich fluids into the subsurface. If regional carbonates formed via this mechanism, it must have occurred early in Martian history, when a thicker CO_2 -rich atmosphere was likely to be present. The surface of Syrtis Major (composed of the youngest

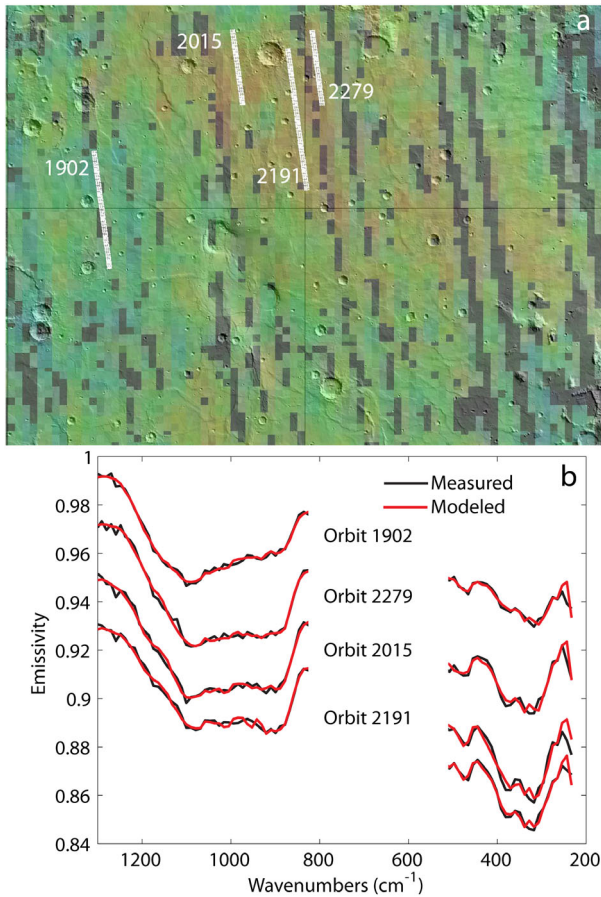


Figure 10. Spectral mixture analysis of TES spectra covering Syrtis Major. (a) Index from Figure 3 overlaid on MOLA shaded relief map. Positions of individual TES orbits are shown. The index map covers the range 60°–80°E, 0°–16.5°N. (b) Atmospherically corrected surface and modeled surface spectra for each orbit. Spectra are offset for clarity. Spectral mixture analysis results are given in Table 4.

lava flows) is early Hesperian in age, so any magmas that fed those lava flows would have interacted with a pre-existing regional subsurface carbonate layer.

[32] If carbonate-magma interactions and the resulting carbonate devolatilization did occur at depth, it is important to assess the impact of the released CO₂ on the properties of the evolving magma, the local geology, and the global climate. On Earth, typical byproducts of Ca-carbonate-magma interactions include Ca-rich pyroxene, plagioclase, and the calc-silicate phases melilite, (Ca,Na)₂(Al,Mg,Fe⁺⁺)(Si,Al)₂O₇, and larnite, Ca₂SiO₄, [e.g., Michaud, 1995; Deegan et al., 2010]. Oxides or hydroxides of Ca and Mg, which are the first products of carbonate devolatilization are relatively rare but do occur, sometimes in xenoliths [e.g., Sabine and Young, 1975; Barberi and Leoni, 1980; Irran et al., 1997]. Lime, especially would be an unlikely component on the Martian surface due to the fact that it recarbonates quickly under a large range of pCO₂ conditions [Abanades and Alvarez, 2003], but portlandite, which is stable under a wide range of conditions, is the primary phase found by our spectral mixture analysis models.

[33] Experiments have shown that calcite assimilation by hydrated basaltic magmas results in the favored crystallization of Ca-rich clinopyroxene over other phases [Marziano et al., 2008]. Perhaps not coincidentally, Syrtis Major has the highest concentration of Ca-rich clinopyroxene of any large low-albedo region on Mars [Rogers and Christensen, 2007]. Enrichment of Ca-bearing silicates would occur if subsurface carbonate was fully assimilated by the ascending magma. Preservation of carbonate decomposition products like those described here requires that subsurface carbonates are thermally metamorphosed without reacting with silicate liquids and brought to the surface. This is consistent with the local inverse correlation we see between the modeled abundances of carbonate decomposition products and high-calcium pyroxene (Table 4). Alternatively, assimilated carbonates might greatly increase the fCO₂ of the magma, resulting in the crystallization of magmatic calcite [e.g., Freda et al., 2010], which would later be thermally metamorphosed by lava flows or impact processes [e.g., Carr, 1989]. Finally, carbonate xenoliths might be brought to the Martian surface, where as described above, they could be decarbonated by further volcanic activity or impact processes. There is evidence in the Martian meteorites that impact-induced decarbonation has, in fact, occurred. Although the cumulate orthopyroxene composition of AHL84001 [Mittlefehldt, 1994] differs considerably from that of the lavas that compose Syrtis Major, it provides several examples of likely carbonate decomposition. Periclase detected in ALH84001 using transmission electron microscopy has been interpreted as evidence for thermal decomposition of Mg-rich carbonates in the meteorite [Barber and Scott, 2003, 2006]. Zolotov and Shock [2000] suggest impact-related dissociation of Fe-carbonates resulted in fine-grained magnetite hydrocarbons found in the meteorite, and Greenwood and McSweeney [2001] also invoke carbonate decomposition in the petrogenetic history of ALH84001. In each case, though, carbonate decomposition products are minor components.

[34] Entrainment or assimilation of carbonates at depth may also have resulted in structural changes in Syrtis Major. Hiesinger and Head, [2004] suggested, based on wrinkle ridge patterns and topographic analysis of Syrtis Major, that portions of the summit collapsed and slid to the southeast, perhaps due to gravitational instabilities or magma chamber inflation [Crumpler et al., 1996]. Mechanical weakening of the subsurface as a result of carbonate devolatilization is another mechanism that could explain the topography and wrinkle ridge patterns on Syrtis Major. A terrestrial analog of this phenomenon is Mount Etna, Italy, which is underlain by a thick carbonate and clay-rich sedimentary sequence.

Table 4. Results of Spectral Mixture Analysis of Syrtis Major Spectra From Four Different Orbits

Mineral Group	Orbit 2191	Orbit 2015	Orbit 2279	Orbit 1902
Pyroxene	14.5 ± 3.1	17.9 ± 4.2	24.6 ± 3.3	27.7 ± 2.9
Feldspar	25.1 ± 2.1	28.0 ± 2.7	25.0 ± 2.4	20.1 ± 2.3
Olivine	19.2 ± 1.2	12.1 ± 3.3	15.0 ± 1.1	10.5 ± 1.0
High-silica Phases	16.9 ± 2.3	14.8 ± 3.4	11.1 ± 1.1	13.9 ± 1.7
Carb. Decomp. Prod.	15.7 ± 1.4	15.5 ± 1.8	10.8 ± 2.0	9.6 ± 1.2
Sulfate	1.6 ± 0.5	2.1 ± 0.7	4.8 ± 0.9	9.5 ± 0.9
Carbonate	6.5 ± 0.9	7.9 ± 1.1	5.5 ± 0.9	6.9 ± 0.8
Quartz	1.4 ± 0.7	1.8 ± 0.8	3.3 ± 0.6	1.8 ± 0.5

The main magma body that feeds the volcano lies within these sediments [Lundgren *et al.*, 2004; Bonaccorso *et al.*, 2010], and numerical modeling has shown that rocks in contact with the magma chamber are heated to 1000°C [Del Negro *et al.*, 2009]. Experiments performed on a marly limestone similar to the rocks that underlie Mount Etna show that the unconfined compressive strength of the rock decreases substantially as a result of devolatilization of clay and carbonate as temperature is steadily increased [Mollo *et al.*, 2011]. Thus, this weakened sedimentary layer below Mount Etna may explain the previously recognized structural instability of the flank of the volcano [Borgia *et al.*, 1992; Lundgren *et al.*, 2004; Patanè *et al.*, 2006; Battaglia *et al.*, 2011]. We suggest here that a similar mechanism may have played a role in the summit collapse of Syrtis Major.

[35] Devolatilization of carbonate-bearing rocks would result in the return of CO₂ to the atmosphere, perhaps influencing the Martian climate [Pollack *et al.*, 1987]. Impacts might also return CO₂ to the atmosphere, but this mechanism is probably less efficient than volcanism [Carr *et al.*, 1989]. The total area of visible carbonate outcrops that have been discovered thus far (Figure 1) is minor, but these outcrops, combined with the detection of carbonate decomposition products at Syrtis Major provide indirect evidence for a larger regional subsurface carbonate layer. This represents a potential major sink of atmospheric CO₂ and suggests an aqueous weathering mechanism for the removal of large quantities of CO₂ from the Noachian atmosphere [e.g., Kahn, 1985; Pollack *et al.*, 1987]. The total volume of carbonates that interacted with the Syrtis Major magmas is unconstrained and would depend on the thickness and areal extent of the layer as well as the number, size, and position of dikes, sills, and magma conduits that fed the Syrtis magmas to the surface. The detection of carbonates around the perimeter of Syrtis Major [Ehlmann *et al.*, 2008; Michalski and Niles, 2010; Wray *et al.*, 2011a; Ehlmann and Mustard, 2012] shows that not all carbonates were decomposed and the volume of carbonates that interacted with subsurface magma conduits was probably minor. This leads to the tentative conclusion that, while CO₂ was certainly evolved from the magma-carbonate interaction, the effects on the Hesperian climate were likely minimal.

6. Conclusions and Future Work

[36] We used spectral index mapping, factor analysis and target transformation, and linear spectral mixture analysis to show that Syrtis Major exhibits an anomalous long-wavelength spectral feature in TES data that is best explained by the presence of carbonate decomposition products. Based on the presence of carbonate outcrops exposed by impacts and erosion in the circum-Syrtis region, we suggest that Syrtis major magmas interacted with an extensive subsurface carbonate layer. Interaction of the magma with these subsurface carbonates resulted in thermal metamorphism and assimilation of the carbonates, leading to the presence of the carbonate decomposition products and perhaps also to the high abundances of high-Ca pyroxene in the Syrtis Major lavas. The presence of portlandite as the dominant modeled carbonate decomposition product and the high modeled abundances of high-Ca pyroxene suggest that subsurface carbonates are dominantly Ca-bearing. This

is in contrast to the primarily Mg-bearing carbonates identified by Ehlmann *et al.* [2008] in Nili Fossae and the Fe/Ca-bearing carbonates identified by Wray *et al.* [2011a] and Michalski and Niles [2010] south and West of Syrtis Major. Subsurface carbonate devolatilization may also be responsible for collapse and transport of Syrtis Major summit material to the southeast. While carbonate devolatilization would have resulted from the interaction of Syrtis Major lavas with a subsurface carbonate layer, the amount of CO₂ returned to the Martian atmosphere as a result of this process is highly unconstrained.

[37] Syrtis Major has the strongest spectral signature of carbonate decomposition products on Mars, but global mapping also revealed potential detections in several other low-albedo regions including Tyrrhena Terra, Terra Cimmeria, and Thaumasia Planum (Figures 4 and 9). Further investigations of these sites are warranted to determine if processes similar to those described in Syrtis Major occurred elsewhere on Mars.

[38] **Acknowledgments.** The authors thank Francis McCubbin and Andrea Harrington for assistance in preparing the CaO sample. They also thank Hap McSween and Paul Niles for discussions of an early version of the manuscript and Joshua Bandfield and Vincenzo Orofino for constructive reviews that improved the content and clarity of the manuscript.

References

- Abanades, J. C., and D. Alvarez (2003), Conversion limits in the reaction of CO₂ with lime, *Energy & Fuels*, **17**, 308–315.
- Abramov, O., and D. A. Kring (2005), Impact-induced hydrothermal activity on early Mars, *J. Geophys. Res.*, **110**(E12), E12S09, doi:10.1029/2005JE002453.
- Bandfield, J. L. (2002), Global mineral distributions on Mars, *J. Geophys. Res.*, **107**(E6), 5042, doi:10.1029/2001JE001510.
- Bandfield, J. L., and M. D. Smith (2003), Multiple emission angle surface-atmosphere separations of thermal emission spectrometer data, *Icarus*, **161**, 47–65.
- Bandfield, J. L., P. R. Christensen, and M. D. Smith (2000a), Spectral data set factor analysis and end-member recovery: Application to analysis of Martian atmospheric particulates, *J. Geophys. Res.*, **105**(E4), 9573–9587, doi:10.1029/1999JE001094.
- Bandfield, J. L., V. E. Hamilton, and P. R. Christensen (2000b), A global view of Martian surface compositions from MGS-TES, *Science*, **287**, 1626–1630.
- Bandfield, J. L., K. S. Edgett, and P. R. Christensen (2002), Spectroscopic study of the Moses Lake dune field, Washington: Determination of compositional distributions and source lithologies, *J. Geophys. Res.*, **107**, 5092, doi:10.1029/2000JE001469.
- Bandfield, J. L., T. D. Glotch, and P. R. Christensen (2003), Spectroscopic identification of carbonate minerals in the Martian dust, *Science*, **301**, 1084–1087.
- Barber, D. J., and E. R. D. Scott (2004), Transmission electron microscopy of minerals in the Martian meteorite Allan Hills 84001, *Met. Planet. Sci.*, **38**, 831–848.
- Barber, D. J., and E. R. D. Scott (2006), Shock and thermal history of Martian meteorite Allan Hills 84001 from transmission electron microscopy, *Met. Planet. Sci.*, **41**, 643–662.
- Barberi, F., and L. Leoni (1980), Metamorphic carbonate ejecta from Vesuvius plinian eruptions: Evidence of the occurrence of shallow magma chambers, *Bull. Volcanol.*, **43**, 107–120.
- Battaglia, M., M. Di Bari, V. Acocella, and M. Neri (2011), Dike emplacement and flank instability at Mount Etna: Constrains from a poro-elastic-model of flank collapse, *J. Volcanol. Geotherm. Res.*, **199**, 153–164.
- Bibring, J.-P., et al. (2005), Mars surface diversity as revealed by the OMEGA/Mars Express observations, *Science*, **307**, 1576–1581.
- Bonaccorso, A., G. Currenti, C. Del Negro, and E. Boschi (2010), Dike deflection modeling for inferring magma pressure and withdrawal, with application to Etna 2001 case, *Earth Planet. Sci. Lett.*, **293**, 121–129.
- Borgia, A., L. Ferrari, and G. Pasquarè (1992), Importance of gravitational spreading in the tectonic and volcanic evolution of Mount Etna, *Nature*, **357**, 231–235.
- Boynton, W. V., et al. (2009), Evidence for calcium carbonate at the Mars Phoenix landing site, *Science*, **325**, 61–64.

- Brown, A. J., S. J. Hook, A. M. Baldridge, J. K. Crowley, N. T. Bridges, B. J. Thomson, G. M. Marion, C. R. deSouza, and J. L. Bishop (2010), Hydrothermal formation of clay-carbonate alteration assemblages in the Nili Fossae region of Mars, *Earth Planet. Sci. Lett.*, **297**, 174–182.
- Bullock, M. A., and J. M. Moore (2007), Atmospheric conditions on early Mars and the missing layered carbonates, *Geophys. Res. Lett.*, **34**, L19201, doi:10.1029/2007GL030688.
- Carr, M. H. (1989), Recharge of an early atmosphere of Mars by impact-induced release of CO₂, *Icarus*, **79**, 311–327.
- Che, C., and T. D. Glotch (2012), The effect of high temperatures on the mid-to-far-infrared emission and near-infrared reflectance spectra of phyllosilicates and natural zeolites: Implications for Martian exploration, *Icarus*, **218**, 585–601.
- Christensen, P. R., et al. (2000a), Detection of crystalline hematite mineralization on Mars by the thermal emission spectrometer: Evidence for near-surface water, *J. Geophys. Res.*, **105**(E4), 9623–9642.
- Christensen, P. R., J. L. Bandfield, V. E. Hamilton, D. A. Howard, M. D. Lane, J. L. Piatek, S. W. Ruff, and W. L. Stefanov (2000b), A thermal emission spectral library of rock-forming minerals, *J. Geophys. Res.*, **105**(E4), 9735–9739.
- Christensen, P. R., et al. (2001), Mars Global Surveyor Thermal Emission Spectrometer experiment: Investigation description and surface science results, *J. Geophys. Res.*, **106**, 23,823–23,871.
- Cloutis, E. A., M. A. Craig, R. V. Kruzelecky, W. R. Jamroz, A. Scott, F. C. Hawthorne, and S. A. Mertzman (2008), Spectral reflectance properties of minerals exposed to simulated Mars surface conditions, *Icarus*, **195**, 140–168.
- Crumpler, L. S., J. W. Head, and J. C. Aubele (1996), Calderas on Mars: Characteristics, structure, and associated flank deformation, *Geol. Soc. Spec. Pub.*, **110**, 307–348.
- Deegan, F. M., V. R. Troll, C. Freda, V. Misiti, J. P. Chadwick, C. L. McLeod, and J. P. Davidson (2010), Magma-carbonate interaction processes and associated CO₂ release at Merapi Volcano, Indonesia: Insights from experimental petrology, *J. Petrol.*, **51**, 1027–1051.
- Del Negro, C., G. Currenti, and D. Scandura (2009), Temperature-dependent viscoelastic modeling of ground deformation: Application to Etna volcano during the 1993–1997 inflation period, *Phys. Earth Planet. Inter.*, **172**, 299–309.
- Ehlmann, B. L., and J. F. Mustard (2012), An in situ record of major environmental transitions on early Mars at Northeast Syrtis Major, *Geophys. Res. Lett.*, **39**, L11202, doi:10.1029/2012GL051594.
- Ehlmann, B. L., et al. (2008), Orbital identification of carbonate-bearing rocks on Mars, *Science*, **322**, 1828–1832.
- Fairen, A. G., et al. (2010), Noachian and more recent phyllosilicates in impact craters on Mars, *Proc. Natl. Acad. Sci.*, **107**, 12095–12100.
- Freda, C., M. Gaeta, B. Giaccio, F. Marra, D. Palladino, P. Scarlato, and G. Sottili (2010), CO₂-driven large mafic explosive eruptions: The Pozzolane Rosse case study from the Colli Albani Volcanic District (Italy), *Bull. Volcanol.*, **73**, 241–256.
- Friedlander, L. R., T. Glotch, J. R. Michalski, T. G. Sharp, M. D. Dyar, and D. L. Bish (2012), Spectroscopic studies of nontronite after impacts at 3 pressures, *Lunar Planet. Sci. XLIII*, abstract 2520.
- Gillespie, A. R. (1992), Enhancement of multispectral thermal infrared images: Decorrelation contrast stretching, *Remote. Sens. Environ.*, **42**, 147–155.
- Glotch, T. D., and J. L. Bandfield (2006), Determination and interpretation of surface and atmospheric Miniature Thermal Emission Spectrometer spectral end-members at the Meridiani Planum landing site, *J. Geophys. Res.*, **111**(E12), E12S06, doi:10.1029/2005JE002671.
- Glotch, T. D., R. V. Morris, P. R. Christensen, and T. G. Sharp (2004), Effect of precursor mineralogy on the thermal infrared emission spectra of hematite: Application to Martian hematite mineralization, *J. Geophys. Res.*, **109**, E07003, doi:10.1029/2003JE002224.
- Greenwood, J. P., and H. Y. McSween (2001), Petrogenesis of Allan Hills 84001: Constraints from impact-melted feldspathic and silica glasses, *Met. Planet. Sci.*, **36**, 43–61.
- Halevy, I., M. T. Zuber, and D. P. Schrag (2007), A sulfur dioxide climate feedback on early Mars, *Science*, **318**, 1903–1907.
- Hamilton, V. E. (2000), Thermal infrared spectroscopy of the pyroxene mineral series, *J. Geophys. Res.*, **105**(E4), 9701–9716.
- Hiesinger, H., and J. W. Head III (2004), The Syrtis Major volcanic province, Mars: Synthesis from Mars Global Surveyor data, *J. Geophys. Res.*, **109**, E01004, doi:10.1029/2003JE002143.
- Irran, E., E. Tillmans, and G. Hentschel (1997), Ternesite, Ca₅(SiO₄)₂SO₄, a new mineral from the Ettringer Bellerberg/Eifel, Germany, *Mineral Petrol.*, **60**, 121–13.
- Johnson, J. R., F. Hörz, P. G. Lucey, and P. R. Christensen (2002), Thermal infrared spectroscopy of experimentally shocked anorthosite and pyroxenite: Implications for remote sensing of Mars, *J. Geophys. Res.*, **107**(E10), 5073, doi:10.1029/2001JE001517.
- Kahn, R. (1985), The evolution of CO₂ on Mars, *Icarus*, **62**, 175–190.
- Koeppen, W. C., and V. E. Hamilton (2008), Global distribution, composition, and abundance of olivine on the surface of Mars from thermal infrared data, *J. Geophys. Res.*, **113**(E5), E05001, doi:10.1029/2007JE002984.
- Lane, M. D., and P. R. Christensen (1997), Thermal infrared emission spectroscopy of anhydrous carbonates, *J. Geophys. Res.*, **102**, 25581–25592.
- Lundgren, P., F. Casu, M. Manzo, A. Pepe, P. Berardino, E. Sansosti, and R. Lanari (2004), Gravity and magma induced spreading of Mount Etna volcano revealed by satellite radar interferometry, *Geophys. Res. Lett.*, **31**, L04602, doi:10.1029/2003GL018736.
- Malinowski, E. R. (1991), *Factor Analysis in Chemistry*, 2nd Ed., John Wiley, Hoboken, N. J.
- Marziano, G. I., F. Gaillard, and M. Pichavant (2008), Limestone assimilation by basaltic magmas: An experimental re-assessment and application to Italian volcanoes, *Contrib. Mineral. Petrol.*, **155**, 719–738.
- Mellon, M. T., B. M. Jakosky, H. H. Kieffer, and P. R. Christensen (2000), High resolution thermal inertia mapping from the Mars Global Surveyor Thermal Emission Spectrometer, *Icarus*, **148**, 437–455.
- Michalski, J. R., and P. B. Niles (2010), Deep crustal carbonate rocks exposed by meteor impact on Mars, *Nature Geosci.*, **3**, 751–755.
- Michalski, J. R., M. D. Kraft, T. Diedrich, T. G. Sharp, and P. R. Christensen (2003), Thermal emission spectroscopy of the silica polymorphs and considerations for remote sensing of Mars, *Geophys. Res. Lett.*, **30**(19), 2008, doi:10.1029/2003GL018354.
- Michalski, J., F. Poulet, J. P. Bibring, and N. Mangold (2010), Analysis of phyllosilicate deposits in the Nili Fossae region of Mars: Comparison of TES and OMEGA data, *Icarus*, **206**, 269–289.
- Michaud, V. (1995), Crustal xenoliths in recent hawaiites from Mount Etna, Italy: Evidence for alkali exchanges during magma-wall rock interaction, *Chem. Geol.*, **122**, 21–42.
- Mittlefehldt, D. W. (1994), ALH84001, a cumulate orthopyroxenite member of the Martian meteorite clan, *Meteoritics*, **29**, 214–221.
- Mollo, S., S. Vinciguerra, G. Iezzi, A. Iarocci, P. Scarlato, M. J. Heap, and D. B. Dingwell (2011), Volcanic edifice weakening via devolatilization reactions, *Geophys. J. Inter.*, **186**, 1073–1077.
- Morris, R. V., et al. (2010), Identification of carbonate-rich outcrops on Mars by the Spirit rover, *Science*, **329**, 421–444.
- Morse, S. A. (1996), Kiglapait mineralogy: 3. Olivine compositions and Rayleigh fractionation models, *J. Petrol.*, **37**(5), 1037–1061.
- Mukhin, L. M., A. P. Koscheyev, Y. P. Dikov, J. Huth, and H. Wanke (1996), Experimental simulations of the photodecomposition of carbonates and sulphates on Mars, *Nature*, **379**, 141–143.
- Mustard, J. F., S. Erard, J.-P. Bibring, J. W. Head, S. Hartz, Y. Langevin, C. M. Pieters, and C. J. Sotin (1993), The surface of Syrtis Major: Composition of the volcanic substrate and mixing with altered dust and soil, *J. Geophys. Res.*, **98**, 3387–3400.
- Niles, P. B., L. A. Leshin, and Y. Guan (2005), Microscale carbon isotope variability in ALH84001 carbonates and a discussion of possible formation environments, *Geochim. et Cosmochim. Acta*, **69**(11), 2931–2944.
- Orofino, V., J. Goldspiel, I. Carofalo, A. Blanco, S. Fonti, and G. A. Marzo (2009), Evaluation of carbonate abundance in putative Martian paleolake basins, *Icarus*, **200**, 426–435.
- Patanè, D., G. Barberi, O. Cocina, P. De Gori, and C. Chiarabba (2006), Time-resolved seismic tomography detects magma intrusions at Mount Etna, *Science*, **313**, 821–823.
- Pollack, J. B., J. F. Kasting, S. M. Richardson, and K. Poliakov (1987), The case for a warm, wet climate on early Mars, *Icarus*, **71**, 203–224.
- Presley, M. A., and P. R. Christensen (1997), Thermal conductivity measurements of particulate materials. 2. Results, *J. Geophys. Res.*, **102**, 6551–6566, doi:10.1029/97JE03303.
- Quinn, R., A. P. Zent, and C. P. McKay (2006), The photochemical stability of carbonates on Mars, *Astrobiology*, **6**, 581–591.
- Ramsey, M. S., and P. R. Christensen (1998), Mineral abundance determination: Quantitative deconvolution of thermal emission spectra, *J. Geophys. Res.*, **103**(B1), 577–596.
- Rogers, A. D. (2011), Crustal compositions exposed by impact craters in the Tyrrhena Terra region of Mars: Considerations for Noachian environments, *Earth Planet. Sci. Lett.*, **301**, 353–364.
- Rogers, A. D., and R. Fergason (2011), Regional-scale stratigraphy of surface units in Tyrrhena and Iapygia Terrae, Mars: Insights into highland crustal evolution and alteration history, *J. Geophys. Res.*, **116**, E08005, doi:10.1029/2010JE003772.
- Rogers, A. D., and O. Aharonson (2008), Mineralogical composition of sands in Meridiani Planum determined from Mars Exploration Rover data and comparison to orbital measurements, *J. Geophys. Res.*, **113**(E6), E06S14, doi:10.1029/2007JE002995.
- Rogers, A. D., and P. R. Christensen (2007), Surface mineralogy of Martian low-albedo regions from MGS-TES data: Implications for upper crustal evolution and surface alteration, *J. Geophys. Res.*, **112**, E01003, doi:10.1029/2006JE002727.

- Rogers, A. D., J. L. Bandfield, and P. R. Christensen (2007), Global spectral classification of Martian low-albedo regions with Mars Global Surveyor Thermal Emission Spectrometer (MGS-TES) data, *J. Geophys. Res.*, *112*, E02004, doi:10.1029/2006JE002726.
- Ruff, S. W. (2004), Spectral evidence for zeolite in the dust on Mars, *Icarus*, *168*, 131–143.
- Ruff, S. W., and P. R. Christensen (2007), Basaltic andesite, altered basalt, and a TES-based search for smectite clay minerals on Mars, *Geophys. Res. Lett.*, *34*, L10204, doi:10.1029/2007GL029602.
- Ruff, S. W., P. R. Christensen, P. W. Barbera, and D. L. Anderson (1997), Quantitative thermal emission spectroscopy of minerals: A laboratory technique for measurement and calibration, *J. Geophys. Res.*, *102*(B7), 14,899–14,913.
- Sabine, P. A., and B. R. Young (1975), Metamorphic processes at high temperature and low pressure: The petrogenesis of the metasomatized and assimilated rocks of Carneal, Co. Antrim, *Phil. Trans. Royal Soc. London, A*, *280*, 225–269.
- Sharp, T. G., J. R. Michalski, M. D. Dyar, D. L. Bish, L. R. Friedlander, and T. Glotch (2012), Effects of shock metamorphism on phyllosilicate structures and spectroscopy, *Lunar Planet. Sci. XLIII*, abstract 2806.
- Stalport, F., Y. Y. Guan, N. Audrey, P. Coll, C. Szopa, F. Macari, A. Person, D. Chaput, F. Raulin, and H. Cottin (2010), Uvolution, a photochemistry experiment in low earth orbit: Investigation of the photostability of carbonates exposed to Martian-like UV radiation conditions, *Planet. Space Sci.*, *58*, 1617–1624.
- Stockstill, K. R., J. E. Moersch, S. W. Ruff, A. Baldrige, and J. Farmer (2005), Thermal Emission Spectrometer hyperspectral analyses of proposed paleolake basins on Mars: No evidence for in-place carbonates, *J. Geophys. Res.*, *110*(E10), E10004, doi:10.1029/2004JE002353.
- Stockstill, K. R., J. E. Moersch, H. Y. McSween, J. Piatek, and P. R. Christensen (2007), TES and THEMIS study of proposed paleolake basins within the Acolis quadrangle of Mars, *J. Geophys. Res.*, *112*(E1), E01001, doi:10.1029/2005JE002517.
- Thomson, J. L., and J. W. Salisbury (1993), The midinfrared reflectance of mineral mixtures (7–14 μm), *Remote. Sens. Environ.*, *45*, 1–13.
- Viviano, C. E., J. E. Moersch, and H. Y. McSween (2012), Spectral evidence for the carbonation of serpentine in Nili Fossae, Mars, *Lunar Planet. Sci. XLIII*, abstract 2682.
- Wray, J. J., S. L. Murchie, B. L. Ehlmann, R. E. Milliken, K. D. Seelos, E. Z. Noe Dobrea, J. F. Mustard, and S. W. Squyres (2011a), Evidence for regional deeply buried carbonate-bearing rocks on Mars, *Lunar Planet. Sci. XLIII*, abstract 2635.
- Wray, J. J., S. L. Murchie, B. L. Ehlmann, R. E. Milliken, J. L. Bishop, K. D. Seelos, E. Z. Noe Dobrea, J. F. Mustard, and S. W. Squyres (2011b), Orbital evidence for iron or calcium carbonates on Mars, *EPSC, Vol. 6*, abstract 1719.
- Wyatt, M. B., V. E. Hamilton, H. Y. McSween, P. R. Christensen, and L. A. Taylor (2001), Analysis of terrestrial and Martian volcanic compositions using thermal emission spectroscopy: 1. Determination of mineralogy, chemistry, and classification strategies, *J. Geophys. Res.*, *106*(E7), 14,711–14,732.
- Zolotov, M. Y., and E. L. Shock (2000), An abiotic origin for hydrocarbons in the Allan Hills 84001 martian meteorite through cooling of magmatic and impact-generated gases, *Met. Planet. Sci.*, *35*, 629–638.